Magnetic Resonance Imaging 115 (2025) 110252

Contents lists available at ScienceDirect

Magnetic Resonance Imaging

journal homepage: www.elsevier.com/locate/mri

Bayesian merged utilization of GRAPPA and SENSE (BMUGS) for in-plane accelerated reconstruction increases fMRI detection power

Chase J. Sakitis, Daniel B. Rowe *

Mathematical and Statistical Sciences, Marquette University, 1313 W Wisconsin Ave, Milwaukee 53233, WI, USA

ARTICLE INFO

Keywords:
Bayesian
fMRI
GRAPPA
Reconstruction
SENSE

ABSTRACT

In fMRI, capturing brain activity during a task is dependent on how quickly the *k*-space arrays for each volume image are obtained. Acquiring the full *k*-space arrays can take a considerable amount of time. Under-sampling *k*-space reduces the acquisition time, but results in aliased, or "folded," images after applying the inverse Fourier transform (IFT). GeneRalized Autocalibrating Partial Parallel Acquisition (GRAPPA) and SENSitivity Encoding (SENSE) are parallel imaging techniques that yield reconstructed images from subsampled arrays of *k*-space. With GRAPPA operating in the spatial frequency domain and SENSE in image space, these techniques have been separate but can be merged to reconstruct the subsampled *k*-space arrays more accurately. Here, we propose a Bayesian approach to this merged model where prior distributions for the unknown parameters are assessed from *a priori k*-space arrays. The prior information is utilized to estimate the missing spatial frequency values, unalias the voxel values from the posterior distribution, and reconstruct into full field-of-view images. Our Bayesian technique successfully reconstructed simulated and experimental fMRI time series with no aliasing artifacts while decreasing temporal variation and increasing task detection power.

1. Introduction

1.1. Background

Functional Magnetic Resonance Imaging (fMRI) is a medical imaging technique that was developed in the early 1990's as a technique to noninvasively observe human brain activity without exogenous contrast agents [1]. This technique detects changes in the blood oxygenation using the blood-oxygen-level dependent (BOLD) contrast [2] when a neuron fires in its proximity. This BOLD contrast can then be used to map brain activity [3]. The magnetic resonance imaging (MRI) scanner measures arrays of complex-valued spatial frequencies called *k*-space [4] which are transformed into brain images using an inverse Fourier transform (IFT). The reconstructed brain images are made up of complex-valued voxels which contain the signal intensity (magnitude) and a measure of local magnetic field (phase) for each pixel in the image.

Despite the phase images generally being discarded using only the magnitude images for fMRI analysis, the phase images are utilized for this research. Producing magnitude and phase images is simply a conversion to polar coordinates from Cartesian coordinates in the complex plane. For this research, the concentration will be on Cartesian *k*-space sampling, with the conversion to polar coordinates used for image depiction purposes.

In fMRI, obtaining hundreds of volume images is necessary to statistically detect activation which of the same underlying volume measured individually through time. Measuring full *k*-space arrays for all slices required to form volume images takes a considerable amount of time due to the size of a dataset from a single experiment. This lengthy acquisition time limits the temporal resolution of the reconstructed images which can diminish the ability to capture brain activity. A great deal of work has been dedicated to reducing the scan time of the fMRI process by accelerating the number of images acquired per unit of time using parallel imaging techniques [5,6,7].

1.2. Previous approaches

With the introduction of parallel imaging techniques, the focus of research has been to acquire more images per unit of time by measuring less data without losing the ability to form a full field-of-view (FOV) reconstructed image. With these techniques, multiple receiver coils are utilized to fully sampled *k*-space data arrays in parallel instead of using the historically used single channel receiver coil. Utilization of multiple

* Corresponding author.
E-mail address: danielrowe@marquette.edu (D.B. Rowe).

https://doi.org/10.1016/j.mri.2024.110252
Received 18 July 2024; Received in revised form 4 September 2024; Accepted 10 October 2024
Available online 16 October 2024

receiver coils allows researchers to skip lines of the *k*-space arrays during the acquisition process yielding subsampled spatial frequency arrays for each coil. This reduces the acquisition time of the *k*-space arrays, but causes the images, after using the IFT, to be aliased, or appear "folded over." The multiple aliased coil images are required to be unaliased and combined into a single, full FOV, reconstructed brain image.

There are two common parallel imaging techniques that accomplish this: GeneRalized Autocalibrating Partial Parallel Acquisition (GRAPPA) [5] and SENSitivity Encoding (SENSE) [7]. GRAPPA operates on the subsampled *k*-space prior to the IFT by assessing localized weights that are used to interpolate the unacquired spatial frequencies for each coil. SENSE operates in image space after the IFT utilizing estimated coil sensitivities (coil weightings) to unalias and combine the aliased coil measurements into a single FOV image.

For the GRAPPA method, once the unacquired spatial frequencies are interpolated, the full coil spatial frequency arrays (acquired plus estimated) are combined into a single *k*-space array by averaging the coil spatial frequency values at each location. The averaged, full *k*-space array is transformed into a brain image using the IFT. GRAPPA is a widely used parallel reconstruction technique and is effective with low acceleration factors since it does not rely on sensitivity coil information. However, GRAPPA has its deficiencies at higher acceleration factors, such as low image quality, a low SNR, and diminished task detection power [8]. Also, since GRAPPA averages the full coil *k*-space arrays, this technique does not incorporate the coil sensitivities resulting in markedly lower overall signal intensity for each voxel [9]. We developed a Bayesian approach to GRAPPA that will incorporate more prior information to estimate the unacquired spatial frequencies [10]. This yields increased SNR and image quality, with improved power in task detection compared to GRAPPA.

The SENSE method uses complex-valued linear regression with a fixed design matrix and a least squares solution to estimate the voxel values of the single, reconstructed brain image. This approach for parameter estimation can be difficult because the complex-valued design matrix can be ill-conditioned. This can cause aliasing artifacts, low image quality, and signal-to-noise ratio (SNR) degradation in the final reconstructed image, which has led to variations of the traditional technique [11,12,13,14]. These variations have deficiencies that hardly mitigate the limitations of the traditional maximum likelihood SENSE procedure. We have previously developed a Bayesian approach to SENSE (BSENSE) that incorporates more prior information and does not use a single *a priori* fixed complex-valued sensitivity matrix [15]. When comparing BSENSE to SENSE, the results yielded no aliasing artifacts with increased SNR, image quality, and improved task detection results [15].

In this paper, we first introduce a merged utilization of GRAPPA and SENSE (MUGS) for in-plane accelerated image reconstruction, though it could be used for through-plane. This technique we are introducing is a two-step reconstruction process. First, GRAPPA is used to estimate the unacquired spatial frequencies resulting in full coil *k*-space arrays. These *k*-space arrays are reconstructed into coil-weighted brain images using the IFT. Then the coil-weighted images are combined into a single, complex-valued brain image using coil sensitivites via SENSE. This process utilizes information from both the spatial frequency domain and the image space domain to reconstruct the subsampled coil *k*-space arrays into a single full FOV brain image.

Despite this merged utilization of both traditional reconstruction techniques operating in both the *k*-space domain and the image domain, it does not take advantage of all valuable available prior information that can be incorporated into the reconstructed image. Here, we propose a Bayesian approach to MUGS (BMUGS) that applies BGRAPPA and BSENSE in place of GRAPPA and SENSE, respectively. In this paper, we illustrate how the BMUGS technique out performs the MUGS technique through a simulation study and their application to experimental data. The simulation and experimental studies performed for this paper are both in fMRI analysis but this methodology can also be applied to diffusion weighted imaging [16].

1.3. Overview

The second section of this paper explains the research problem that arises from subsampling *k*-space data and discusses the model of the MUGS image reconstruction technique. This will lead into our proposed Bayesian approach to MUGS presented in Section 3. Section 4 shows results from the simulation study comparing the MUGS and BMUGS techniques. Section 5 presents a similar comparison with experimental task fMRI data. In Section 6, we conclude with an overview of the results from the simulation and experimental studies and discuss future work.

2. MUGS technique

2.1. Research problem

From the single channel coil, full *k*-space arrays are acquired along a trajectory as shown in Fig. 1a. In fMRI, the most common acquisition pattern is Echo Planar Imaging (EPI) and is used for the acquisition of the experimental data used in this paper. The trajectory follows a Cartesian path with turnaround points at the end of each row. These complex-valued spatial frequency arrays are then reconstructed into full FOV complex-valued brain images.

Since the objective of parallel imaging is to allow for subsampling of *k*-space, Fig. 1b shows the trajectory for undersampling the spatial frequencies. Like the fully sampled *k*-space array in Fig. 1a, the scanner starts in the bottom left and moves across the row acquiring complex-valued spatial frequency points along the row. Then, when it gets to the end of the row, instead of moving up to the next row, it skips lines according the acceleration factor n_A. With an acceleration factor of $n_A = 3$, we see that in Fig. 1b, the trajectory skips the next two lines acquiring the third line above the bottom. This process is repeated until all designated rows of the discretized subsampled *k*-space array is acquired. This subsampling pattern reduces the amount of acquired spatial frequencies by the acceleration factor. For example, subsampling a 96×96 array with $n_A = 3$, the *k*-space array then reduces to a 32×96 dimension for each slice.

Instead of a single channel coil, $n_C > 1$ receiver coils are utilized in parallel to allow for subsampling the spatial frequency arrays. An example of a four-channel coil alignment can be arranged with the first coil located at the anterior, second at the right lateral, third at the posterior, and fourth at the left lateral (clockwise rotation). The coil sensitivity profiles used in the simulation and experimental studies of this paper overlap, as they typically do in coil configuration. With $n_A = 3$, each coil acquires subsampled *k*-space as depicted on the left side of Fig. 2. The right side of Fig. 2 displays the aliased brain image for each coil after using the IFT. These coil brain images are rendered useless from the aliasing so parallel image techniques are utilized to unfold and combine them into a single composite brain image that can be used for analysis.

2.2. Reconstruction process

As mentioned in 1.2, multiple steps are required to properly merge both GRAPPA and SENSE together. Fig. 3 demonstrates the flowchart of how the subsampled spatial frequencies are reconstructed into a single brain image using this MUGS technique. In Fig. 3, there are Autocalibration Signal (ACS) spatial frequency arrays in step 1 that are utilized for estimating the localized weights, W_c, for GRAPPA and the coil sensitivities, S, for SENSE (step 2). To calculate the weights used for interpolation in GRAPPA, a kernel with k_{row} rows and k_{col} columns is placed around the acquired spatial frequency points closest to the ACS point. The points inside the kernel, along with the ACS point, are then used to calculate the weights via least squares. Step 3 of the process is then to acquire the subsampled *k*-space arrays for the fMRI experiment.

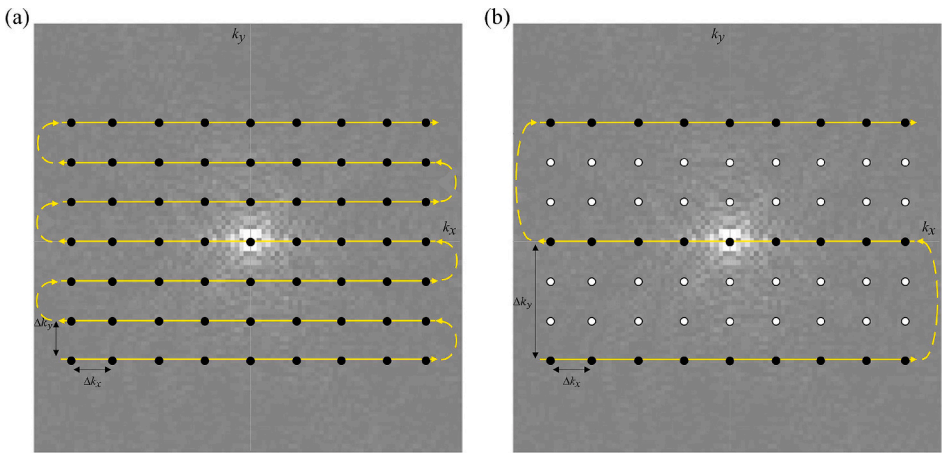

Fig. 1. Trajectories of a fully sampled k-space array (a) and a subsampled k-space array with an acceleration factor of $n_A = 3$ (b).

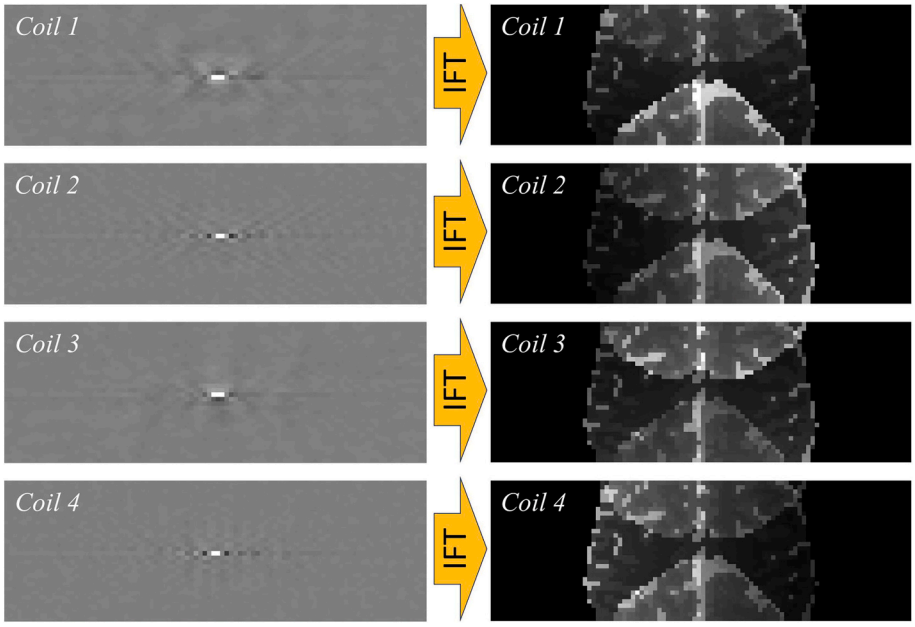

Fig. 2. Illustration of $n_C = 4$ subsampled coil k-space arrays with an acceleration of $n_A = 3$ (left) and their respective aliased brain images after the IFT (right).

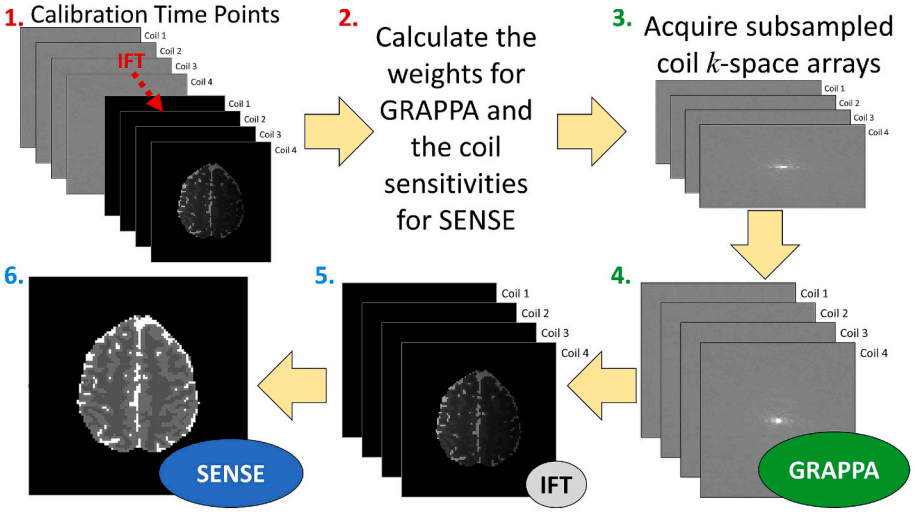

Fig. 3. Flow chart for the MUGS model for image reconstruction.

All the unacquired spatial frequencies are estimated using GRAPPA yielding full coil *k*-space arrays in step 4. The coil *k*-space arrays are then inverse Fourier transformed to coil-weighted images (step 5). Then SENSE reconstruction is utilized to weight and combine the coil images into a single composite brain image in step 6. This process is repeated at each time point in the subsampled time series of coil spatial frequency arrays.

The model for MUGS begins with the GRAPPA model. That is

$$f_{ec}^{(\omega)} = W_c^{(\omega)} f_{kc}^{(\omega)} + \eta_{ec}^{(\omega)}, \tag{2.1}$$

where $\omega = 1, \ldots, K$, $f_{ec} \in \mathbb{C}^{n_C \times 1}$ represents the complex-valued interpolated *k*-space values, $f_{kc} \in \mathbb{C}^{p \times 1}$ represents the complex-valued acquired *k*-space values, $\eta_c \in \mathbb{C}^{n_C \times 1}$ represents the additive complex-valued noise with $\eta_c \sim N(0, \tau^2(1+i))$, and $p = n_C k_{rows} k_{cols}$. The interpolated spatial frequencies, f_{ec}, are then placed in the respectively locations of the missing *k*-space values resulting in full coil *k*-space arrays, f_{full}.

The full coil *k*-space arrays f_{full} are then inverse Fourier transformed into coil images. The SENSE model is then applied to the full FOV coil image measurements with no acceleration factor, i.e. $n_A = 1$. That is

$$a_c^{(\nu)} = S_c^{(\nu)} \nu_c^{(\nu)} + \varepsilon_c^{(\nu)}, \tag{2.2}$$

where $\nu = 1, \ldots, M$, $a_c \in \mathbb{C}^{n_C \times 1}$ represents the complex-valued coil measurements, $S_c \in \mathbb{C}^{n_C \times 1}$ represents the matrix of complex-valued coil sensitivities, $\nu_c \in \mathbb{C}$ represents the complex-valued unaliased voxel value, $\varepsilon_c \in \mathbb{C}^{n_C \times 1}$ represents the additive complex-valued noise where $\varepsilon_c \sim N(0, \sigma^2(1+i))$, and $M = n_y n_x$ where n_y and n_x are the number of rows and columns, respectively, in the reconstructed image.

3. Bayesian approach to MUGS

3.1. BGRAPPA model

For the BGRAPPA technique, the same linear model as GRAPPA (expressed Eq. 2.1) is used except the acquired spatial frequencies will be the f_{ec} variable instead of the f_{kc} variable. This creates a model where the design matrix and the coefficients can both be treated as unknown parameters, allowing us to take a Bayesian approach to the linear regression. Then the weights, W_c, and the unacquired spatial frequencies, f_{kc}, along with the residual *k*-space variance, τ^2, are treated as unknowns with prior distributions placed on them. We also use an isomorphic real-valued representation of the linear GRAPPA model in Eq. 3.1

$$\begin{bmatrix} f_{eR} \\ f_{eI} \end{bmatrix} = \begin{bmatrix} \boxed{W_R - W_I W_I W_R} \end{bmatrix} \begin{bmatrix} f_{kR} \\ f_{kI} \end{bmatrix} + \begin{bmatrix} \eta_R \\ \eta_I \end{bmatrix}, \quad (\eta_R, \eta_I)' \sim N(0, \tau^2 I_{2n_C}). \tag{3.1}$$

where $f_{eR} \in \mathbb{R}^{n_C \times 1}$ and $f_{eI} \in \mathbb{R}^{n_C \times 1}$ are the real and imaginary components, respectively, of f_{ec}, $W_R \in \mathbb{R}^{n_C \times p}$ and $W_I \in \mathbb{R}^{n_C \times p}$ are the real and imaginary components of W_c, $f_{kR} \in \mathbb{R}^{p \times 1}$ and $f_{kI} \in \mathbb{R}^{p \times 1}$ are the real and imaginary components of f_{kc}, and $\eta_R \in \mathbb{R}^{n_C \times 1}$ and $\eta_I \in \mathbb{R}^{n_C \times 1}$ are the real and imaginary components of η_c. This equation is a latent variable model with complex values and can be more compactly written as $f_e = W f_k + \eta$ where $f_e \in \mathbb{R}^{2n_C \times 1}$, $W \in \mathbb{R}^{2n_C \times 2p}$, $f_k \in \mathbb{R}^{2p \times 1}$, and $\eta \in \mathbb{R}^{2n_C \times 1}$ are the real-valued isomorphic representations of f_{ec}, W_c, f_{kc}, and η_c, respectively.

In the BGRAPPA method, two different representations of the weights will be used. The first representation is the skew-symmetric design matrix W as shown in Eq. 3.1. The second representation is $D = [W_R, W_I]$ which is used in the prior distribution and for parameter estimation of the weights. This ensures that W_R and W_I are uniquely estimated for W and do not need to be duplicated. Because the real and imaginary components of fMRI data have been shown to be normally distributed [17,18], we utilize the normal distribution for the real and imaginary components of the residual spatial frequency error. The data likelihood for the acquired spatial frequencies for the n_C coils is

$$P(f_e | W, f_k, \tau^2) \propto (\tau^2)^{-\frac{2n_C}{2}} exp\left[-\frac{1}{2\tau^2} (f_e - W f_k)'(f_e - W f_k) \right]. \tag{3.2}$$

Available prior information about the unacquired spatial frequencies f_k, the weights W, and the residual *k*-space variance τ^2 can be quantified with assessed hyperparameters of prior distributions. For the prior distributions, the unacquired spatial frequencies f_k are specified to have a normal prior distribution (Eq. 3.3), the weights D are specified to have a normal prior distribution (Eq. 3.4), and the *k*-space noise variance τ^2 is specified to have an inverse gamma prior distribution (Eq. 3.5). That is

$$P(f_k | n_k, f_{k0}, \tau^2) \propto (\tau^2)^{\frac{-2p}{2}} exp\left[-\frac{n_k}{2\tau^2} (f_k - f_{k0})'(f_k - f_{k0}) \right], \tag{3.3}$$

$$P(D | n_w, D_0, \sigma^2) \propto (\tau^2)^{\frac{-2n_C p}{2}} exp\left[-\frac{n_w}{2\tau^2} tr(D - D_0)(D - D_0)' \right], \tag{3.4}$$

$$P(\tau^2 | \alpha_k, \delta) \propto (\tau^2)^{-(\alpha_k + 1)} exp\left[-\frac{\delta}{\tau^2} \right], \tag{3.5}$$

where tr is the trace of the $(D - D_0)(D - D_0)'$ matrix. The ACS spatial frequencies are utilized to assess the hyperparameters $n_k, f_{k0}, n_w, D_0, \alpha_k$, and δ, as outlined in [10]. The joint posterior distribution of the unacquired spatial frequencies f_k, the weights W, and the residual *k*-space variance τ^2 is

$$P(f_k, D, \tau^2 | f_e) \propto P(f_e | W, f_k, \tau^2) P(f_k | n_k, f_{k0}, \tau^2) P(D | n_w, D_0, \tau^2) P(\tau^2 | \alpha_k, \delta), \tag{3.6}$$

with the distributions specified from Eqs. 3.2, 3.3, 3.4, and 3.5.

Using the posterior distribution in Eq. 3.6, the priors described in Eqs. 3.3, 3.4, and 3.5, and the likelihood distribution in Eq. 3.2, the Maximum *A Posteriori* (MAP) estimate for the unacquired spatial frequencies f_k, the weights W, and the residual *k*-space variance τ^2 is estimated via the Iterated Conditional Modes (ICM) optimization algorithm [19,20]. Beginning with the prior means for each parameter as initial estimates, the ICM algorithm iterates over the parameters, calculating its posterior conditional mode until convergence at the joint posterior mode. The ICM will produce the global maximum, the MAP, instead of the local maximum since each of the posterior conditionals are unimodal. The posterior conditional modes are

$$\widehat{f}_k = (W'W + n_k I_{2p})^{-1} (W' f_e + n_k f_{k0}), \tag{3.7}$$

$$\widehat{D} = (F_e F_k' + n_w D_0)(F_k F_k' + n_w I_{2p})^{-1}, \tag{3.8}$$

$$\widehat{\tau}^2 = \frac{\Phi}{2(2n_C + 2p + 2n_C p + 1)}, \tag{3.9}$$

where $\Phi = (f_e - W f_k)'(f_e - W f_k) + n_k (f_k - f_{k0})'(f_k - f_{k0}) + \alpha_k \delta + n_w tr[(D - D_0)(D - D_0)']$, $F_e = [f_{eR}, f_{eI}]$ and $F_k \in \mathbb{R}^{2p \times 2}$ is a skew symmetric matrix representation of the unaliased voxel values f_k as expressed by

$$F_k = \begin{bmatrix} \boxed{f_{kR} f_{kI} - f_{kI} f_{kR}} \end{bmatrix}. \tag{3.10}$$

The full conditional posterior distributions of each parameters f_k, D, and τ^2 are given by

$$f_k | W, \tau^2, f_e \sim N\left\{ \widehat{f}_k, \tau^2 (W'W + n_k I_{2p})^{-1} \right\}, \tag{3.11}$$

$$D | f_k, \tau^2, f_e \sim MN\left\{ \widehat{D}, \tau^2 (F_k' F_k + n_w I_{2p})^{-1} \right\}, \tag{3.12}$$

$$\tau^2 | f_k, W, f_e \sim IG\{\alpha_{k^*}, \delta_*\}, \tag{3.13}$$

where $\alpha_{k^*} = n_C p + n_C + p + \alpha_k$ and $\delta_* = [(f_e - Wf_k)'(f_e - Wf_k) + n_k(f_k - f_{k0})'(f_k - f_{k0}) + n_W tr((D - D_0)(D - D_0)') + 2\delta]/2$.

3.2. BSENSE model

For the BSENSE technique, the same linear model as SENSE (Eq. 2.2) is used. Similar to BGRAPPA, there are two different representations of the coil sensitivities. The first representation is $S \in \mathbb{R}^{2n_C \times 2n_A}$ as demonstrated in Eq. 2.2 is necessary for the proper skew symmetric design matrix for complex-valued multiplication. The second representation is $H = [S_R, \quad S_I]$, used in the prior distribution and ultimately for parameter estimation of the coil sensitivities. This is because S_R and S_I uniquely determine S and do not need to be duplicated. As mentioned above, because the real and imaginary errors have been shown to be normally distributed, we use independent and identically distributed normal errors in the real and imaginary components. The likelihood for the aliased voxel measurements for the n_C coils becomes

$$P(a|S, v, \sigma^2) \propto (\sigma^2)^{-\frac{2n_C}{2}} exp\left[-\frac{1}{2\sigma^2}(a - Sv)'(a - Sv)\right] \quad . \tag{3.14}$$

We can quantify available prior information about the unobserved parameters of the voxel intensities v, the coil sensitivities S, and the residual variance σ^2 in the likelihood with assessed hyperparameters of prior distributions. For the prior distributions, the voxel values v are specified to have a normal distribution (Eq. 3.15), the coil sensitivities H are specified to have a normal distribution (Eq. 3.16), and the noise variance σ^2 is specified to have an inverse gamma distribution (Eq. 3.17).

$$P(v|n_v, v_0, \sigma^2) \propto (\sigma^2)^{-\frac{2n_A}{2}} exp\left[-\frac{n_v}{2\sigma^2}(v - v_0)'(v - v_0)\right] \quad , \tag{3.15}$$

$$P(H|n_S, H_0, \sigma^2) \propto (\sigma^2)^{-\frac{2n_C n_A}{2}} exp\left[-\frac{n_S}{2\sigma^2} tr(H - H_0)'(H - H_0)\right] \quad , \tag{3.16}$$

$$P(\sigma^2|\alpha, \beta) \propto (\sigma^2)^{-(\alpha+1)} exp\left[-\frac{\beta}{\sigma^2}\right], \tag{3.17}$$

where tr is the trace of the $(H - H_0)'(H - H_0)$ matrix. The hyperparameters n_S, H_0, n_v, v_0, α, and β are objectively assessed from the ACS images, as outlined in [15], but can also be determined using a completely subjective approach. The joint posterior distribution of the true slice voxel values v, the coil sensitivities S (and H), and the noise variance σ^2 is

$$P(v, H, \sigma^2|a) \propto P(a|S, v, \sigma^2) P(v|n_v, v_0, \sigma^2) P(H|n_S, H_0, \sigma^2) P(\sigma^2|\alpha, \beta), \tag{3.18}$$

with the distributions specified from Eqs. 3.14, 3.15, 3.16, and 3.17.

Using the posterior distribution in Eq. 3.18, two approaches are used to estimate the unaliased voxel values v, coil sensitivities S, and residual variance σ^2: Maximum *a posteriori* (MAP) estimation using the Iterated Conditional Modes (ICM) optimization algorithm [19,20] to find the joint posterior mode, and marginal posterior mean (MPM) estimation via Markov chain Monte Carlo (MCMC) Gibbs sampling [21,22]. Beginning with the initial estimates of the each parameter, ICM iterates over the parameters, calculating its posterior conditional mode and converges to a maximum of the joint posterior density. Since each of the posterior conditionals are unimodal, the ICM will produce the global maximum, the MAP. The conditional modes are

$$\widehat{v} = (S'S + n_v I_{2n_A})^{-1}(S'a + n_v v_0), \tag{3.19}$$

$$\widehat{H} = (V'V + n_S I_{2n_A})^{-1}(V'Y + n_S H_0), \tag{3.20}$$

$$\widehat{\sigma}^2 = \frac{\Theta}{2(2n_C + 2n_A + \alpha + 2n_C n_A + 1)}, \tag{3.21}$$

where $\Theta = (a - Sv)'(a - Sv) + n_v(v - v_0)'(v - v_0) + \alpha\beta + n_S tr[(H - H_0)(H - H_0)']$, $Y = [a_R, a_I]$ and $V \in \mathbb{R}^{2n_A \times 2}$ is a skew symmetric matrix representation of the unaliased voxel values v as expressed by

$$V = \begin{bmatrix} v_R & v_I \\ -v_I & v_R \end{bmatrix}. \tag{3.22}$$

The full conditional distributions are given by

$$v|S, \sigma^2, a \sim N\left\{\widehat{v}, \sigma^2(S'S + n_v I_{2n_A})^{-1}\right\}, \tag{3.23}$$

$$H|v, \sigma^2, a \sim N\left\{\widehat{H}, \sigma^2(V'V + n_S I_{2n_A})^{-1}\right\}, \tag{3.24}$$

$$\sigma^2|v, S, a \sim IG\{\alpha_*, \beta_*\}, \tag{3.25}$$

where $\alpha_* = n_C n_A + n_C + n_A + \alpha$ and $\beta_* = [(a - Sv)'(a - Sv) + n_v(v - v_0)'(v - v_0) + n_S tr((H - H_0)(H - H_0)') + 2\beta]/2$.

3.3. BMUGS model

For our Bayesian approach to MUGS (BMUGS), we treat the unacquired spatial frequencies f_k, the weights W, the residual k-space variance τ^2, the unaliased voxel values v, the coil sensitivities H, and the residual image variance σ^2 as unknown parameters that are dependent on the acquired spatial frequencies f_e. The priors for each of these parameters (Eqs. 3.3, 3.4, 3.5, 3.15, 3.16, and 3.17) along with the likelihood equations (Eqs. 3.2 and 3.14) are combined to produce the joint posterior distribution as expressed in Eq. 3.26.

$$P(V_k, H, \Sigma, D, F_{k^*}, T|F_{e^*}) \propto P(V_k, H, \Sigma|F_{full}) P(F_{k^*}, D, T|F_{e^*}), \tag{3.26}$$

where $V_k = (v_1, \ldots, v_M)$ represents the vector of unaliased voxel values, $H = I_M \times (H_1, \ldots, H_M)$ represents the matrix of coil sensitivities, $\Sigma = (\sigma_1^2, \ldots, \sigma_M^2)$ represents the vector of residual noise variances, $F_{k^*} = (f_{k1}, \ldots, f_{kL})$ represents the vector of unacquired spatial frequencies, $D = I_L \times (D_1, \ldots, D_L)$ represents the matrix of localized weights, $T = (T_1, \ldots, T_L)$ represents the vector of k-space noise variance, $F_{e^*} = (f_{e1}, \ldots, f_{eJ})$ represents the vector of acquired spatial frequencies, F_{full} represents the vector of the acquired spatial frequencies f_e and the f_k spatial frequencies after interpolation, $M = n_y n_x$, L is the number of unacquired spatial frequencies, and J is the number of acquired spatial frequencies.

The $P(F_{k^*}, D, T|F_{e^*})$ represents the posterior distribution of BGRAPPA and the $P(V_k, H, \Sigma|F_{full})$ represents the posterior distribution of BSENSE. With the BSENSE posterior component being dependent on full coil k-space arrays F_{full}, we must first estimate the unacquired spatial frequency values using BGRAPPA. Then the interpolated spatial frequencies are appended with the acquired spatial frequencies yielding full FOV coil k-space arrays. After applying the IFT to the coil spatial frequency arrays F_{full}, our BSENSE technique is then used to complete the image reconstruction process for BMUGS. The process is the same process illustrated in Fig. 3 except BGRAPPA and BSENSE are used instead of GRAPPA and SENSE, respectively.

The hyperparameter determination for the BGRAPPA component of our BMUGS technique follows the assessment outlined in [10]. The parameter estimation for the BGRAPPA part of BMUGS follows the estimation outlined in Section 3.1. This means that the unacquired spatial frequencies f_k, the localized weights W, and the k-space noise variance τ^2 have the same posterior conditional modes and posterior conditional distributions as expressed in eqs. 3.7, 3.8, 3.9, 3.11, 3.12, and 3.13 respectively.

For the BSENSE part, the hyperparameter determination follows that detailed in [15], and the parameter estimation follows the estimation

process outlined in Section 3.2. For this paper, only the MAP estimate using the ICM was utilized for parameter estimation. Since the coil measurements are full FOV images after the IFT, the acceleration factor would be $n_A = 1$. This makes the posterior conditional modes to be

$$\widehat{v} = (S'S + n_v I_2)^{-1}(S'a + n_v v_0), \tag{3.27}$$

$$\widehat{H} = (V'V + n_S I_2)^{-1}(VY' + n_S H_0), \tag{3.28}$$

$$\widehat{\sigma}^2 = \frac{\Theta}{2(4n_C + \alpha + 3)}, \tag{3.29}$$

where $\Theta = (a - Sv)'(a - Sv) + n_v(v - v_0)'(v - v_0) + \alpha\beta + n_S tr[(H - H_0)(H - H_0)']$, $Y = [a_R, a_I]$ and $V \in \mathbb{R}^{2\times 2}$ is a skew symmetric matrix representation of the unaliased voxel values v as expressed in Eq. 3.22.

With an acceleration factor of one, the posterior conditional distributions become

$$v|S, \sigma^2, a \sim N\left\{\widehat{v}, \sigma^2(S'S + n_v I_2)^{-1}\right\}, \tag{3.30}$$

$$H|v, \sigma^2, a \sim MN\left\{\widehat{H}, \sigma^2(V'V + n_S I_2)^{-1}\right\}, \tag{3.31}$$

$$\sigma^2|v, S, a \sim IG\{\alpha_*, \beta_*\}, \tag{3.32}$$

where $\alpha_* = 2n_C + \alpha + 1$ and $\beta_* = [(a - Sv)'(a - Sv) + n_v(v - v_0)'(v - v_0) + n_S tr((H - H_0)(H - H_0)') + 2\beta]/2$.

4. Simulation study

The software used for this research was MATLAB 2022b run on a 12th Gen Intel(R) Core(TM) i7-1255U laptop computer with 16GB RAM, operating on Windows 11.

4.1. Non-task data

To mimic the experimental data shown in Section 5, a single slice noiseless, non-task image was used to generate two series of 510 simulated full FOV coil images. The magnitude scale of the non-task simulated image was determined by taking the root sum of squares of the cull coil images. This combines the complex-valued coil images into a single, real-valued image yielding the scale for the magnitude. The complex-valued image was multiplied by a designed sensitivity map with $n_C = 8$ coils and replicated $n_{TR} = 510$ times for the 510 repetition times (TR) for both series. The first three images in both the simulated series were appropriately scaled, based on the experimental data, replicating the increased signal due the time it takes for the magnetization to reach a stable state for real-world MRI experiments. The series of images were Fourier transformed into full coil spatial frequency arrays. These series of coil k-space arrays were simulated by adding separate $N(0, 0.0036 n_x n_y)$ noise to both time series to the real and imaginary parts of the coil k-space arrays. This particular noise level corresponds to the noise in the fMRI experimental data used in Section 5. This data generation follows a general linear model with normally distributed noise and no spatial or temporal dependencies.

The last n_{cal} time points of the first time series of non-task images served as ACS images that were utilized for hyperparameter assessment so nothing more done to this time series. The second time series was used as the simulated non-task experiment. After applying noise to the k-space arrays, the first 20 time points of the second series were discarded leaving 490 time points of non-task images for the single slice. This is to mimic the experimental study as those time points are not utilized in the fMRI analysis. However, those time points could be used to estimate T_1 and static magnetic field maps. The remaining 490 time points in the time series were subsampled by censoring lines in k-space according to the different acceleration factors used for the simulation.

4.2. Reconstruction results

To examine the reconstruction performance between BMUGS vs. MUGS, we first reconstructed the subsampled coil k-space measurements at one time point, giving us a single unaliased image for both methods. With an acceleration factors of $n_A = 3$, we evaluated the first time point of the 490 simulated non-task time series, shown in Fig. 4 (left).

From the first 510 non-task full FOV ACS time series, we used the last $n_{cal} = 30$ time points to assess the hyperparameters in both the k-space domain (BGRAPPA/GRAPPA) and the image domain (BSENSE/SENSE). For the BGRAPPA component, the prior means from the ACS information for the unacquired spatial frequency arrays f_{k0} and the localized weights D_0 were used as initial values for f_k and D. These initial values were utilized to generate a τ^2 value from the posterior conditional mode (Eq. 3.9), initializing the ICM optimization algorithm. For the BSENSE component, the prior means from the ACS images, after IFT, for the unaliased voxels v_0 and the sensitivity coils H_0 were used as initial values for v and H. These initial values were utilized to generate a σ^2 value from the posterior conditional mode (Eq. 3.21), initializing the ICM algorithm. For estimating the parameters, the ICM algorithms only needed three iterations before converging. This resulted in having computation times of about 0.50 s per time point for the BGRAPPA component (about 0.16 s for the GRAPPA component of MUGS) and 0.10 s per time point for the BSENSE component (about 0.04 s for the SENSE component of MUGS). Fig. 5 displays the true simulated magnitude and phase images (first column) along with the BMUGS unaliased images (second column), and the MUGS unaliased images (third column).

From a visual standpoint, we can see that the joint MAP estimate from BMUGS produces magnitude and phase images that more closely resemble the true non-aliased magnitude and phase images in Fig. 5 (left column). MUGS, on the other hand, produced an image with a higher noise level and slight bias in the magnitude image compared to our BMUGS technique. This is evident by the noise level in the voxels outside of the brain being markedly higher, which is typically masked out in fMRI studies. Here we retain them to evaluate the spatial noise level of the reconstructed images for both techniques. Unlike the BMUGS and true phase images, the MUGS technique also produced a phase image with no anatomical structure, rendering it essentially unusable. Phase images are commonly discarded in analysis but we use them to further analyze the different reconstruction techniques. Further, using both magnitude and phase images have been shown to yield increased power of activity detection [23,24] and additional biological information outside of the just using magnitude images [25].

Next, we evaluated how different number of ACS time points, n_{cal}, used for hyperparameter assessment affected the reconstructed images. For this analysis, we fixed the acceleration factor to be $n_A = 3$ for subsampling the coil k-space measurements of the simulated non-task time series with $n_{TR} = 490$ time points. For separate hyperparameter assessments, we set the number of ACS time points to be $n_{cal} = 5, 10, 15, 20, 25, 30$ and After hyperparameter determination, the subsampled non-task time series was reconstructed using BMUGS and MUGS.

The results displayed in Fig. 6 show that increasing the number of ACS time points noticeably decreases the noise level outside of the brain for BMUGS but only slightly decreases for the MUGS reconstructed magnitude images. For both techniques, it appears that increasing the ACS time points has negligible effect inside the brain.

To quantify the differences between the true and reconstructed magnitude images inside the brain, we use the mean squared error, $MSE = \frac{1}{K}\sum_{j=1}^{K}(v_j - \overline{v}_j)^2$, where K is the number of voxels inside the brain in the reconstructed image, v_j is the reconstructed magnitude value of

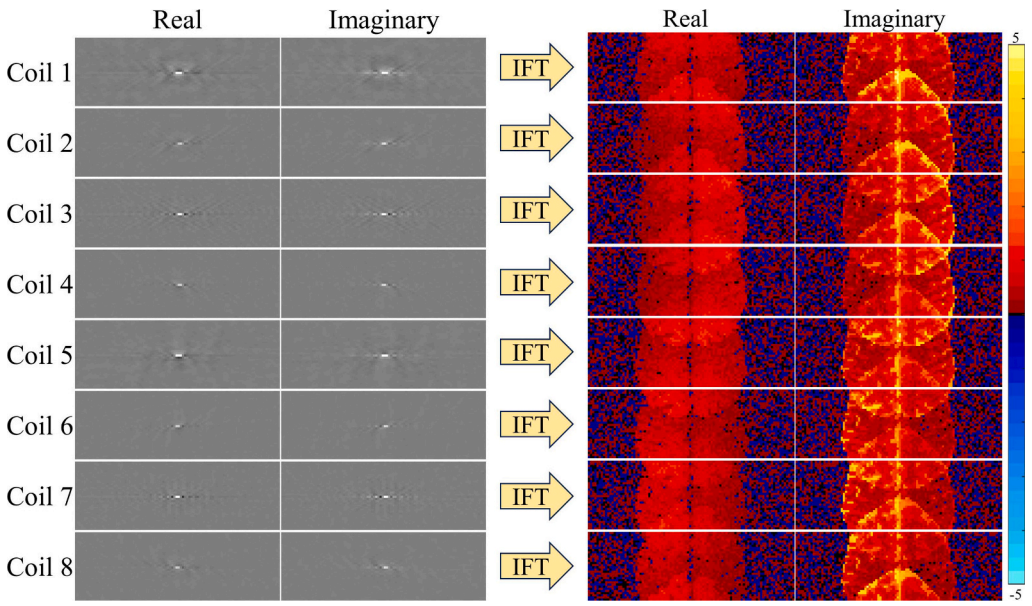

Fig. 4. Real and imaginary simulated noisy subsampled coil *k*-space arrays (left) and the aliased coil images after IFT (right) for first time point in the non-task time series.

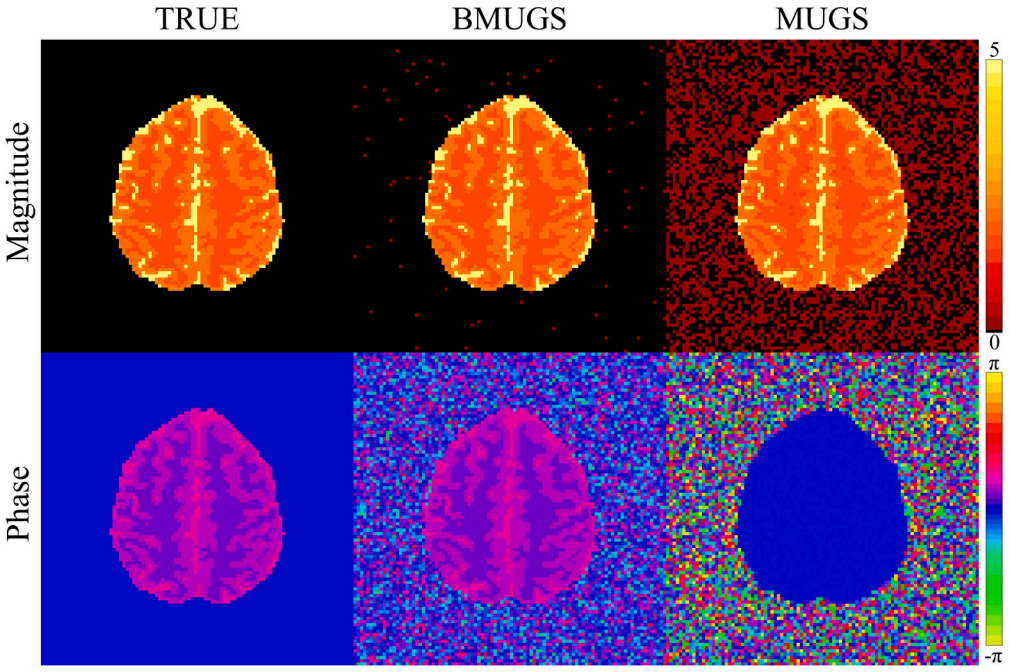

Fig. 5. True non-task unaliased images (first column), BMUGS unaliased non-task images (second column) using ICM, and MUGS non-task images (third column) with magnitude images in the first row and phase images in the second row.

the *j*th voxel, and $\bar{v}_j$ is the true magnitude value of the *j*th voxel. This measure indicates how accurate a reconstructed image is compared to the true simulated image. Having a lower MSE estimate indicates higher accuracy with the reconstructed image. The MSE of inside the brain for both BMUGS and MUGS for each number of ACS time points is displayed in Fig. 7a. The MSE for inside the brain for the BMUGS reconstructed magnitude images is smaller than the MUGS reconstructed magnitude images indicating a more accurate reconstruction.

Along with the MSE, we also evaluated entropy of the reconstructed magnitude images for both techniques. Entropy analyzes uncertainty and smoothness across the entire reconstructed image. Similar to the MSE estimate, lower entropy means less uncertainty throughout the image [26]. The equation for entropy is given by $E = -\sum_{j=1}^{N}\left[\frac{v_j}{v_{max}} ln\left(\frac{v_j}{v_{max}}\right)\right]$, where *ln* is the natural log, *N* is the number of voxels in the reconstructed image, v_j is the reconstructed magnitude value of the *j*th voxel, and v_{max} is the voxel intensity if all the image intensities were in one pixel [1] given by $v_{max} = \sqrt{\sum_{j=1}^{N} v_j^2}$. The results for calculating the entropy for both BMUGS and MUGS using different ACS time points is shown in Fig. 7b. BMUGS appears to have markedly lower entropy as it decreases from 195.7 to 181.6 compared to MUGS which also decreases from 198.9 to 189.6 as the number of ACS time points increases. The phase results for both reconstruction techniques

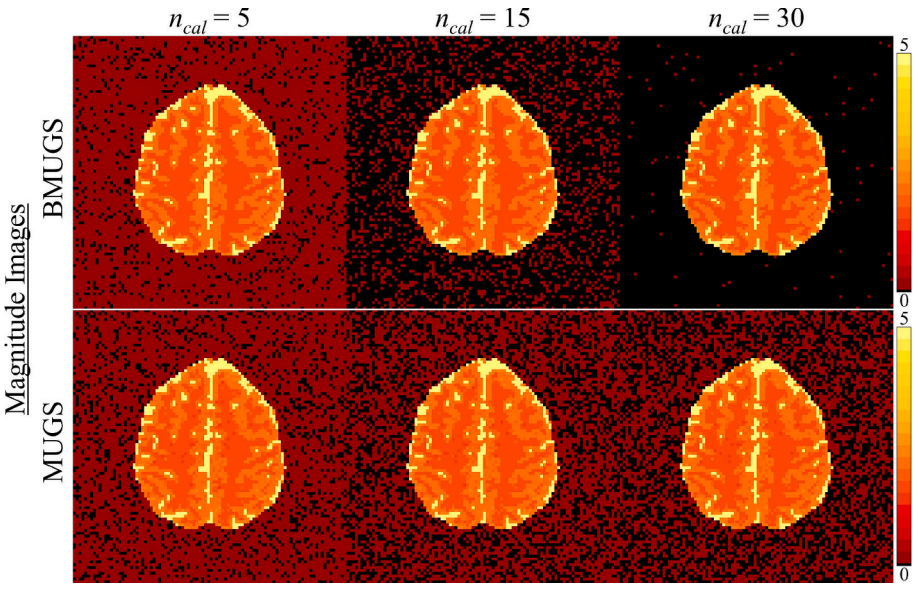

Fig. 6. Reconstructed magnitude images for different number of ACS images using BMUGS estimate (top row) and MUGS (second row).

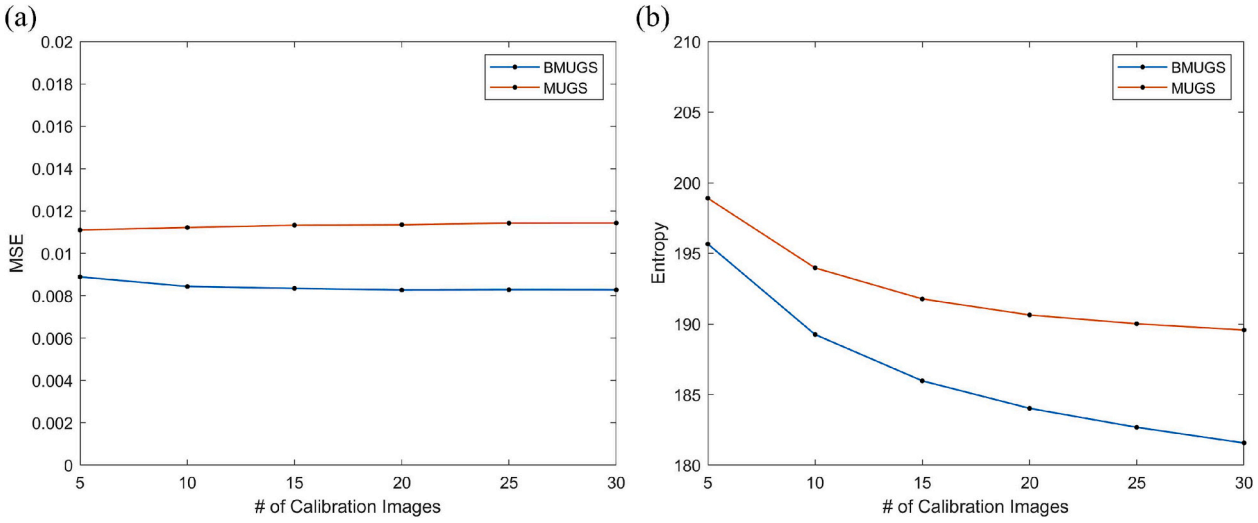

Fig. 7. (a) MSE for inside the brain for BMUGS and MUGS comparing both methods' reconstructed images to the true simulated magnitude image for each number of ACS time points. (b) Entropy plot for BMUGS and MUGS for each number of ACS images. For both plots, BMUGS is shown in red and MUGS is shown in blue. (For interpretation of the references to colour in this figure legend, the reader is referred to the web version of this article.)

using different ACS time points is shown in Section 1 of the Supplementary Material.

To further analyze BMUGS compared to MUGS, we also evaluated how different acceleration factors, n_A, affected the reconstructed images. For this analysis, we fixed the number of ACS time points to be $n_{cal} = 30$ for hyperparameter assessment. Then we set the acceleration factors to be $n_A = 2, 3, 4, 6, 8, 12$ to indicate the subsampling pattern for the non-task time series. These subsampled k-space coil measurements with separate acceleration factors were reconstructed into full FOV images using BMUGS and MUGS with comparisons along the way.

Fig. 8 exhibits the reconstructed magnitude images from BMUGS (top row) and MUGS (bottom row) for different acceleration factors. The results show that the reconstructed magnitude images from BMUGS and MUGS are negligibly affected by increasing the acceleration factor. The reconstructed phase image results for different acceleration factors resemble the results displayed in the bottom row of Fig. 5 and are shown in Section 1 of the Supplementary Material. We also evaluated the temporal variance and SNR images for separate acceleration factors and the results are illustrated in Fig. 9. Note that the scale for the temproal variance for BMUGS (first row) is remarkably smaller than the scale for the temporal variance for MUGS. This indicates that BMUGS has a considerably smaller variance through time. As the acceleration factor increases, the temporal variance for BMUGS decreases while the temporal variance for MUGS remains relative constant inside the brain but decreases outside the brain. With noticeably smaller temporal variance, this yields a considerably higher SNR for BMUGS (third row of Fig. 9) compared to MUGS (fourth row of Fig. 9). This is evident by the scale of the SNR images for BMUGS having a much larger maximum value compared to MUGS. Increasing acceleration factor also markedly increases the SNR for BMUGS (as expected with the decreasing temporal variance) and remains constant for MUGS. With higher SNR values, this shows that BMUGS is largely unaffected by noise compared to MUGS.

4.3. Task activation

In task-based fMRI, a baseline signal value for each voxel is given by

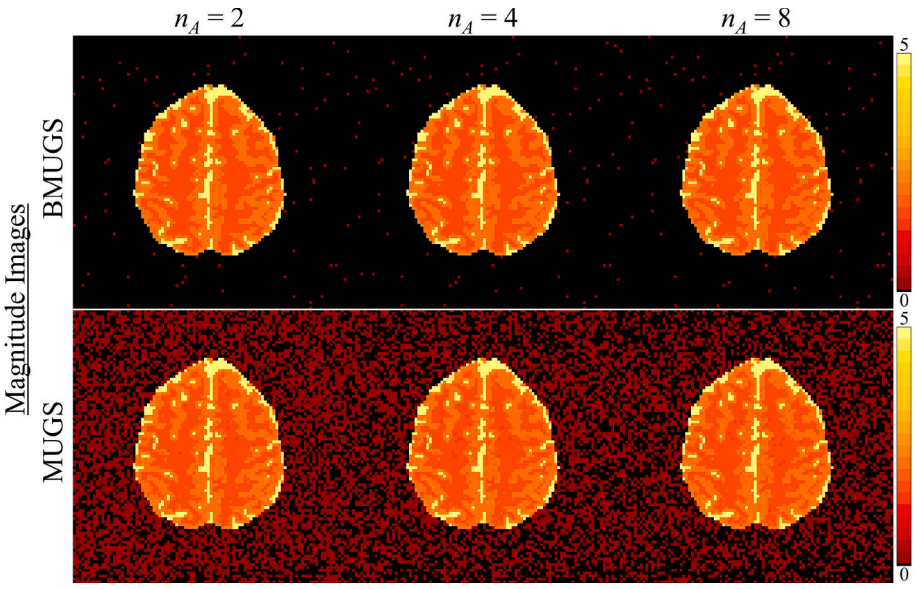

Fig. 8. Reconstructed magnitude images for different acceleration factors using BMUGS (top row) and MUGS (second row).

the non-task reconstructed images, giving us an intercept only simple linear regression $y = \beta_0 + \varepsilon$ where y is the voxel value in the reconstructed image. Adding in task activation to certain images in the series gives us simple linear regression $y = \beta_0 + x\beta_1 + \varepsilon$ for the reconstructed voxel values where β_0 is the baseline voxel value, which determines the SNR $= \beta_0/\sigma$, and β_1 is the estimated signal increase (related to task) from β_0 determining the contrast-to-noise ratio CNR $= \beta_1/\sigma$. The vector $x \in \{0,1\}^{n_{IMG}}$, where n_{IMG} is the number of reconstructed images in the series, is a vector composed of zeros and ones corresponding to the time points in the series without task activation (zero) and time points with task (ones). This can then be written as the linear regression $y = XB + \varepsilon$, where $X = [1, \quad x] \in \mathbb{R}^{n_{IMG} \times 2}$ and $B = [\beta_0, \beta_1]'$.

Typically, the CNR is much smaller than the SNR, rendering the task is not visible on the reconstructed images. Instead, a right-tailed t-test is performed with $H_0 : \beta_1 \leq 0$ and $H_a : \beta_1 > 0$. We only anticipate an increased signal from the task activation which is why our alternative hypothesis is $>$ and not $\neq$. A $\beta_1 = 0.045$ magnitude-only signal increase is added to the true noiseless non-task image to simulate task. With $\varepsilon \sim N(0, 0.0036)$ noise added to the simulated time series, we obtain a CNR of 0.75 showing that the added signal increase is not higher than the noise level. A simulated phase task of $\pi/120$ was also added and analyzed in Section 1 of the Supplementary Material. Since the region of interest (ROI) in the experimental data is in the left motor cortex, we added this simulated task activation in that region. The brain activity from the experimental fMRI is in the left motor cortex because of the unilateral right-hand finger tapping experiment [27] performed during the MRI scan.

4.4. FMRI time series data generation

Along with the same noiseless task image mentioned in Subsection 4.1, a true noiseless task image was used to simulate a series of 510 full FOV coil images for one slice. These true images were multiplied by the same $n_C = 8$ coil sensitivity maps used for the non-task simulated time series (Subsection 4.1), generating coil-weighted brain images. This series of images was Fourier transformed in full coil k-space arrays with $N(0, 0.0036 n_x n_y)$ noise added to the real and imaginary parts of the k-space arrays. To simulate the experimental fMRI data described in Subsection 5.1, the series was generated by starting with 20 non-task time points. The series is then followed by 16 epochs, a stimulation period where the subject is at rest (non-task) or performing an action (task), of 15 non-task and 15 task time points. The series was then finished with 10 non-task time points producing the simulated fMRI series of $n_{TR} = 510$ time points. The scaling for the first few non-task images in the simulated series was the same as the signal increases outlined in Subsection 4.1 for each of the tissue types. The first 20 time points were discarded leaving 490 time points in the series, mimicking the experimental study performed Section 5. The last n_{cal} time points in the non-task time series from Subsection 4.1 were utilized to assess the hyperparameters from full FOV coil ACS time points. For this fMRI simulation, we evaluate task detection results using both BMUGS and MUGS using different acceleration factors, $n_A = 2, 3, 4$. We also evaluated how different ACS time points effect the task detection results but omitted them from this paper as they do not add any extra value that the acceleration factor testing does not have.

4.5. FMRI time series reconstruction results

The hypothesis test described in Subsection 4.3 was carried out to determine which voxels experienced statistically significant signal increase i.e. task activation. The statistically significant voxels from the BMUGS and MUGS reconstructed time series for each acceleration factor were analyzed using the 5 % false discovery rate (FDR) threshold procedure [28,29,30]. The ROI, left motor cortex, consists of 28 voxels with the added simulated task.

Fig. 10 displays the statistically significant voxels for the magnitude-only task detection from the BMUGS reconstructed time series (first row) and the MUGS reconstructed time series (second row) for the separate acceleration factors. The t-statistics are also summarized in Fig. 10 for both reconstruction techniques using each acceleration factor. The results in Fig. 10 show that BMUGS identified more statistically significant voxels in the ROI for each acceleration factor compared to MUGS. For acceleration factors $n_A = 3, 4$, MUGS captures very few active voxels. Analyzing the summary of the t-statistics, we see that the mean value was much higher for BMUGS with a lower standard deviation compared to MUGS for each of the acceleration factors. This demonstrates that BMUGS performs better with its power in task detection. Increasing the acceleration factor does decrease the number of voxels identified and the mean of the t-statistics for both techniques, especially with MUGS.

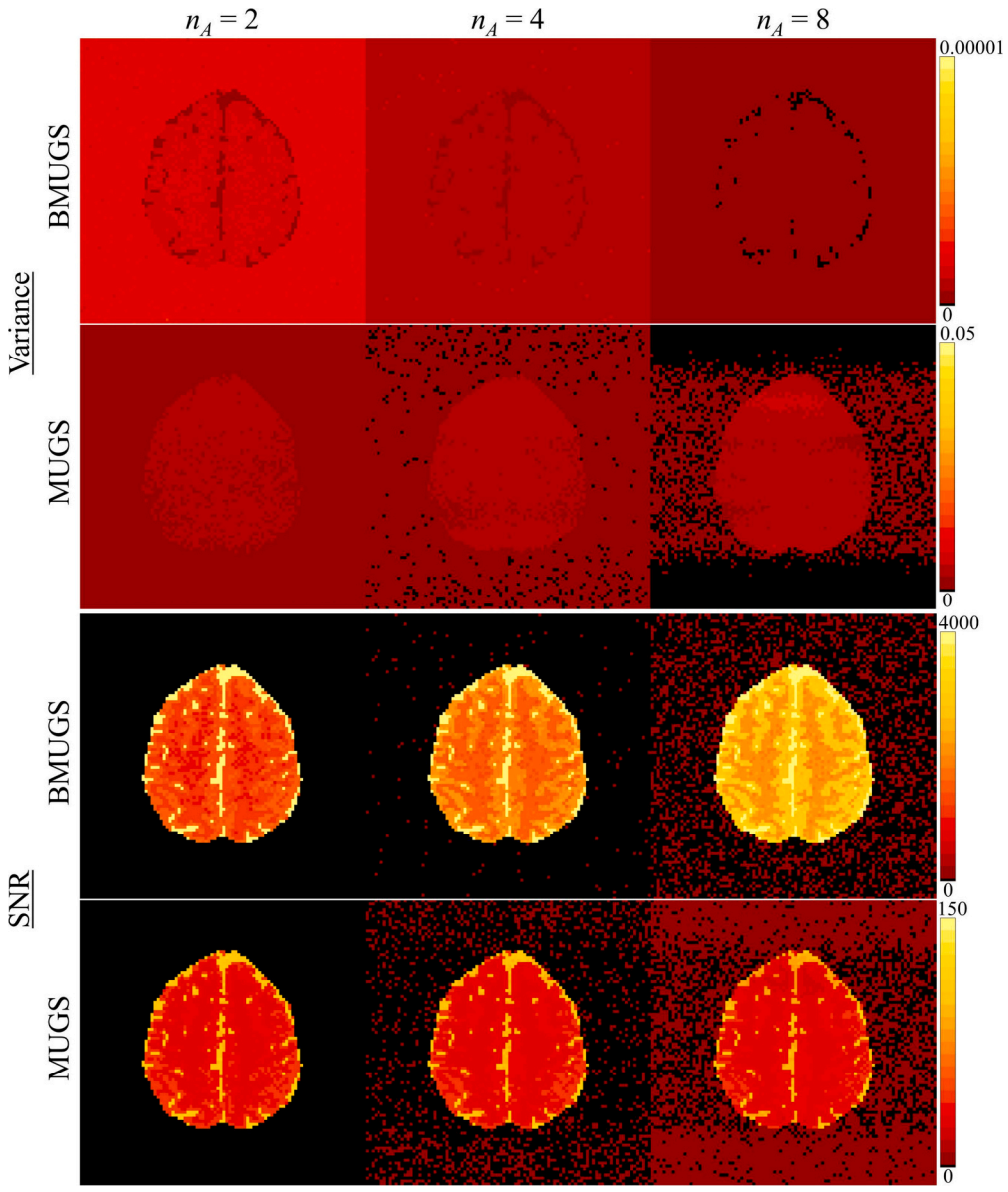

Fig. 9. Temporal variance and SNR images for different acceleration factors using BMUGS (first row and third row, respectively) and MUGS (second row and fourth row, respectively).

5. Experimental study

5.1. Data description

An fMRI experiment on a single subject was conducted using a 3.0 T General Electric Signa LX magnetic resonance imager. This experiment consisted of two time series containing 510 time points each: one non-task and one fMRI series. For each volume image in the experimental series, a time dependent echo time, TE_t, consisted of three parts. The first part was fixed to have a value of $TE = 42.7$ ms at the first 10 time points. In the second part, the next five TE values were an equally spaced interval of values 42.7 ms, 45.2 ms, 47.7 ms, 50.2 ms, and 52.7 ms and was repeated for another 5 time points. For the final part, the last 490 time points were fixed at 42.7 ms. To account for T_1 effects and varying echo times, the center row of k-space for each TR in each receiver coil was acquired with three navigator echoes which is used to correct any potential Nyquist "ghosting." The additional rows of k-space were integrated to estimate and adjust the error in the center frequency and group delay offsets between the odd and even lines of k-space [31].

The last $n_{cal} = 30$ full coil k-space arrays of a non-task series utilized for hyperparameter assessment, similar to the simulated study. After an initial 20 s of rest, a bilateral finger-tapping action was performed in a block design with 16 epochs of 15 s off and 15 s on and concluded with 10 s of rest yielding the series of $n_{TR} = 510$ repetitions. Each repetition in the series was 1 s with a flip angle of 90° and an acquisition bandwidth of 125 kHz. The data was collected using $n_C = 8$ receiver coils obtaining nine 2.5 mm thick axial slices with a 96×96 dimension and a posterior to anterior phase encoding direction.

Typically, the magnetic fields in an fMRI experiment will induce a drift in the phase over time which we correct before reconstruction to give us a stable phase through time. First, the angular phase temporal mean of the time-series is calculated and angularly subtracted for each voxel time-series. A local second order polynomial was spatially fit to the resultant difference of the voxel phase time-series. Then the fitted phase is angularly subtracted from the original producing a steady phase over time for each coil.

For this paper, the time series for the second slice was used to analyze the effects of applying the $n_A = 2, 3, 4$ different acceleration factors for

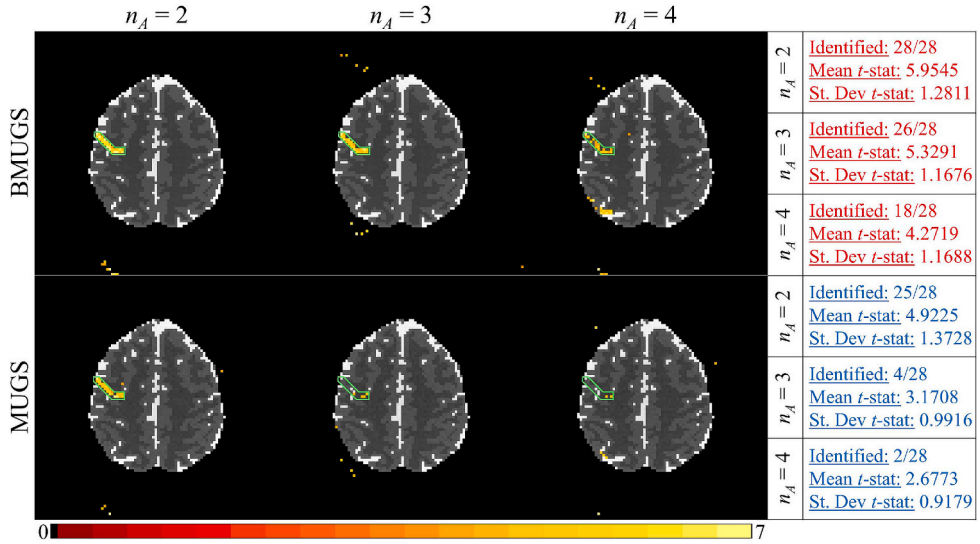

Fig. 10. Statistically significant voxels in the ROI using FDR for BMUGS (first row), significant voxels in the ROI using FDR for MUGS (second row), and analysis of the *t*-statistics in the boxes on the right with BMUGS in red and MUGS in blue. (For interpretation of the references to colour in this figure legend, the reader is referred to the web version of this article.)

both BMUGS and MUGS. Like the simulation study, the subsampled coil spatial frequency arrays came from artificially skipping lines in *k*-space, mimicking the effect of actual subsampling. The first 20 images were discarded due to magnetization stability and varying echo times, leaving $n_{IMG} = 490$ time points for the fMRI experiment. However, the first 10 images of the 20 discarded can be used to estimate a T_1 map [27] and the second 10 images could be used for static magnetic field mapping [32].

5.2. Experimental results

Each image in the entire time series of subsampled coil *k*-space measurements were reconstructed using BMUGS and MUGS separately, similar to the simulation study. The magnitude reconstructed images for both BMUGS (top row) and MUGS (bottom row) of the first time point are displayed in Fig. 11 for each acceleration factor. The results in Fig. 11 show that BMUGS reconstruction produced clearer, less noisy images compared to MUGS. Inside the brain, it is noticeable when analyzing the reconstructed images using $n_A = 3, 4$ acceleration factors (columns 3 and 4) but is apparent outside the brain for each n_A.

To quantify the differences inside the brain, MSE estimates were used to compare the reference image and reconstructed images. The MSE for BMUGS was approximately 0.015 for each acceleration factor. For MUGS, the MSEs inside the brain were 0.052, 0.103, and 0.145 for acceleration factors 2, 3, 4, respectively. This means MUGS had an 247 %, 587 %, and 867 % larger MSE inside the brain for each acceleration factor, respectively, than BMUGS. These results reflect the lesser noise from the BMUGS reconstructed magnitude images compared to MUGS. The entropy for BMUGS (191.1, 191.3, and 191.4, respectively) was also lower than the entropy for MUGS (201.9, 200.1, 198.8) indicating less uncertainty for each reconstructed image.

For detecting task activation, the hypothesis test outlined in Subsection 4.3 was carried out, similar to Subsection 4.5. Fig. 12 displays the statistically significant voxels for BMUGS (top row) and MUGS (bottom row) using the 5 % FDR threshold. The summary of the *t*-statistics for both BMUGS (red) and MUGS (blue) are also shown in Fig. 12. With the ROI containing 28 voxels that experience task activation, BMUGS correctly detected more active voxels than MUGS for all three acceleration factors. Our BMUGS technique also had a much higher mean *t*-statistic and lower standard deviation for all the acceleration factors. With task detection being the primary objective of fMRI, these

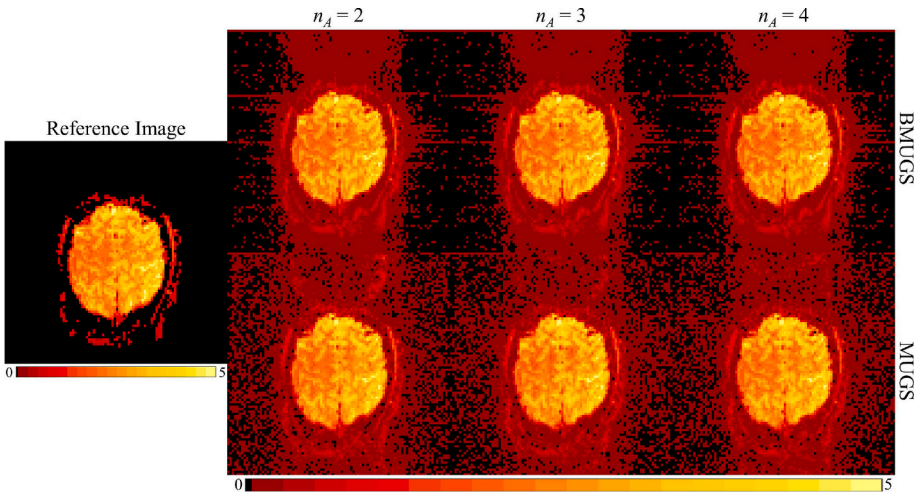

Fig. 11. BMUGS unaliased non-task magnitude images for each acceleration factor (first row), and MUGS unaliased non-task magnitude images for each acceleration factor (second row) with the magnitude reference image (left).

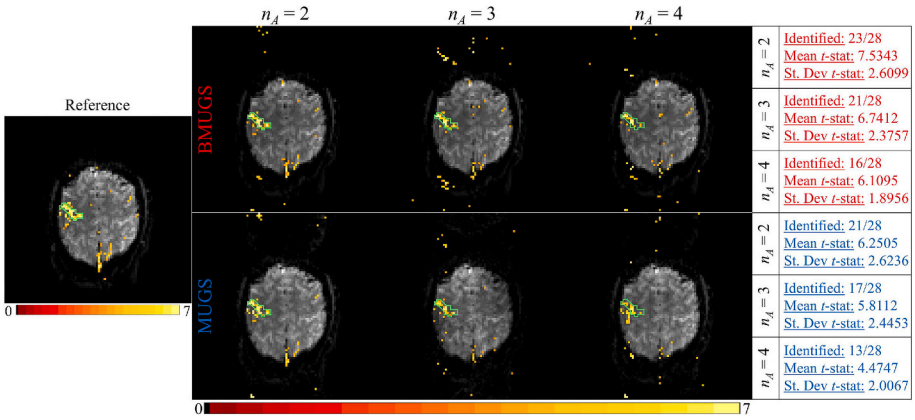

Fig. 12. Statistically significant voxels in the ROI using FDR for BMUGS reconstructed images (first row) for three different acceleration factors, significant voxels in the ROI using FDR for MUGS (second row) for three different acceleration factors, and analysis of the *t*-statistics to the right of the images with BMUGS in red and MUGS in blue. (For interpretation of the references to colour in this figure legend, the reader is referred to the web version of this article.)

results show that BMUGS is the superior reconstruction technique compared to MUGS.

6. Discussion

Parallel imaging techniques have become very common in fMRI for reducing scan time and capturing brain activity. These techniques reconstruct subsampled *k*-space data, which is unusable, into full FOV brain images which can be utilized for fMRI analysis. Subsampling *k*-space data sets allows for practitioners to increase the number of slices or images in the series, reconstruct higher resolution images, or a combination of both in the same time it takes to acquired fully sampled *k*-space. The importance of time determines the acceleration factor while the coil configuration is determined by what configurations the facility possesses.

Applying an acceleration factor in an fMRI experiment can significantly reduce the acquisition time of spatial frequency arrays and volume images. However, taking the IFT of the subsampled *k*-space arrays yields aliased coil images. SENSE and GRAPPA are common reconstruction techniques that reconstruct these subsampled *k*-space arrays or aliased coil images into full FOV brain images. GRAPPA estimates the unacquired spatial frequencies that are skipped during the acquisition of the subsampled *k*-space arrays yielding full FOV coil spatial frequency arrays. These coil spatial frequency arrays are then averaged together and inverse Fourier transformed to get a single composite brain image. However, GRAPPA has its drawbacks which include reduced signal intensities, low image quality, low SNR, and weakened task detection power at higher acceleration factors. The reduced signal intensities are due to GRAPPA not utilizing coil sensitivity information in its reconstruction process. In SENSE image reconstruction, the aliased coil images are simultaneously unaliased and combined, resulting in a single composite brain image. This image reconstruction method can be difficult in the presence of an ill-conditioned design matrix. Here, we include a model that merges both GRAPPA and SENSE (MUGS) since GRAPPA operates in the spatial frequency domain and SENSE operates in the image domain. Despite this merged model, there are still discrepancies with applying this model as valuable prior information that can incorporated into the image reconstruction is discarded.

Hence, we introduce a Bayesian approaches to MUGS which utilizes previously addressed methods of BSENSE and BGRAPPA. Using more available information from the ACS spatial frequencies and images to assess the hyperparameters, our proposed Bayesian approach successfully reconstructed a series of simulated non-task images without any aliasing artifacts. Our BMUGS technique also showed to have numerous improvements over the reconstructed images of the MUGS techniques when applied to both simulated and experimental fMRI data. With BMUGS exhibiting superior results compared to MUGS, fMRI research could benefit on a larger scale with contributions to the human connectome project.

Both BMUGS and MUGS does not incorporate denoising or smoothing techniques either during or after the reconstruction process. These techniques are commonly used techniques in fMRI for reducing spatial noise in the images and enhancing the assessment of task activation. Extension of denoising and spatial smoothing techniques to these reconstruction process can be considered for future work of this research for a full comprehensive reconstruction process. These reconstruction techniques can be further analyzed by mixing the BMUGS and MUGS processes. This can be done by using GRAPPA to estimate the unacquired spatial frequencies and BSENSE to combine the coil images and vice versa.

This paper used the full posterior distribution for reconstructing images, meaning available prior information was quantified on all six parameters (f_k, D, τ^2 ν, S, and σ^2) and utilized for parameter estimation. Only the MAP estimate using the ICM algorithm for both the BGRAPPA component and the BSENSE component was used to reconstruct the time series for both the simulated and experimental studies. We also considered using a Gibbs sampling algorithm to estimate the unknown parameters as this would yield in entire posterior distribution for each parameter. We did not run the Gibbs sampler for practicality reasons since it is more computationally expensive compared to the ICM algorithm. There is still value in running a Gibbs sampler as it has the additional benefit of quantifying uncertainty. For instance, it could be utilized on a shorter series of images, provide us more statistical information about any voxel, or for hypothesis testing between two images. It is possible to hybridize the ICM and Gibbs sampler with a couple of ICM steps followed by a short or no-burn Gibbs sampler. We can also hybridize by using the ICM for the BGRAPPA component and Gibbs sampling for the BSENSE component or vice versa.

Our proposed procedure can also be repeated for vertical aliasing as opposed to the horizontal aliasing used here. In Section 1.2, we mention that MUGS (and BUMGS) can be utilized as a simultaneous multi-slice (SMS) image reconstruction technique. We can further test these models by comparing to other SMS technqiues [33,34,35]. In this paper, a magnitude-only activation model was utilized to detect task activation. In Section 1.3 of Supplementary Material, phase-only activation for BMUGS and MUGS is analyzed with the results showing strong task detection power for the BMUGS technique. Since the reconstructed images are complex-valued, our proposed model is expected to be

applicable for complex activation models for task detection [36,23,24].

CRediT authorship contribution statement

Chase J. Sakitis: Writing – original draft, Visualization, Software, Investigation, Formal analysis. **Daniel B. Rowe:** Writing – review & editing, Supervision, Resources, Project administration, Methodology, Formal analysis, Conceptualization.

Declaration of competing interest

None declared.

Acknowledgments

The authors thank the Wehr Foundation as this research was funded by the Computational Sciences Summer Research Fellowship (CSSRF) at Marquette University in the Department of Mathematical and Statistical Sciences. This research was also funded by the Regular Research Grant (RRG) provided by the Committee on Research at Marquette University.

Appendix A. Supplementary data

Supplementary data to this article can be found online at https://doi.org/10.1016/j.mri.2024.110252.

References

[1] Bandettini P, Jesmanowicz A, Wong E, Hyde JS. Processing strategies for time-course data sets in functional MRI of the human brain. Magn Reson Med 1993;30(2):161–73.
[2] Ogawa S, Lee TM, Nayak AS, Glynn P. Oxygenation-sensitive contrast in magnetic resonance image of rodent brain at high magnetic fields. Magn Reson Med 1990;14(1):68–78.
[3] Ogawa S, Tank DW, Ravi M, Ellermann JM, Kim SG, Merkle H, et al. Intrinsic signal changes accompanying sensory stimulation: functional brain mapping with magnetic resonance imaging. Proc Natl Acad Sci 1992;89(13):5951–5.
[4] Kumar A, Welti D, Ernst RR. NMR Fourier zeugmatography. J Magn Reson 1975;18(1):69–83.
[5] Griswold MA, Jakob PM, Heidemann RM, Nittka M, Jellus V, Wang J, et al. Generalized autocalibrating partially parallel acquisition (GRAPPA). Magn Reson Med 2002;47(6):1202–10.
[6] Hyde JS, Jesmanowicz A, Froncisz W, Kneeland JB, Grist TM, Campagna NF. Parallel image acquisition from noninteracting local coils. J Magn Reson 1986;70(3):512–7.
[7] Pruessmann KP, Weiger M, Scheidegger MB, Boesiger P. SENSE: sensitivity encoding for fast MRI. Mag Reson Med 1999;42(5):952–62.
[8] Deshmane A, Gulani V, Griswold MA, Seiberlich N. Parallel MR imaging. Magn Reson Imaging 2012;36(1):55–72.
[9] Sakitis CJ. Formal Bayesian approaches to the sense and grappa parallel FMRI reconstruction techniques along with their combination. ProQuest Dissert Theses 2024;150. https://www.proquest.com/dissertations-theses/formal-bayesian-approaches-sense-grappa-parallel/docview/3045048784/se-2.
[10] Sakitis CJ, Rowe DB. A Bayesian approach to GRAPPA parallel fMRI image reconstruction increases SNR and power of task detection. Ann Appl Stat 2024. In Press.
[11] King KF, Angelos L. SENSE image quality improvement using matrix regularization. In: Proceedings of the 9th Annual Meeting of ISMRM, 1771; 2001.
[12] Liang ZP, Bammer R, Ji J, Pelc NJ, Glover GH. Making better SENSE: Wavelet denoising, Tikhonov regularization, and total least squares. In: Proceedings of the 10th Annual Meeting of ISMRM, 2388; 2002.
[13] Lin FH, Kwong KK, Belliveau JW, Wald LL. Parallel imaging reconstruction using automatic regularization. Magn Reson Med 2004;51(3):559–67.
[14] Liu B, King K, Steckner M, Xie J, Sheng J, Ying L. Regularized sensitivity encoding (SENSE) reconstruction using Bregman iterations. Magn Reson Med 2009;61(1):145–52.
[15] Sakitis CJ, Brown DA, Rowe DB. A Bayesian complex-valued latent variable model applied to functioncal magnetic resonance imaging. J Royal Stat Soc, Series C 2024. https://doi.org/10.1093/jrsssc/qlae046.
[16] Moon WJ, Lee MH, Chung EC. Diffusion-weighted imaging with sensitivity encoding (SENSE) for detecting cranial bone marrow metastases: comparison with T1-weighted images. Korean J Radiol 2007;8(3):185–91.
[17] Henkelman RM. Measurement of signal intensities in the presence of noise in MR images. Med Phys 1985;12(2):232–3.
[18] Lindquist MA. The statistical analysis of fMRI data. Stat Sci 2008;23(4):439–64.
[19] Lindley DV, Smith AFM. Bayes estimates for the linear model. J Royal Stat Soc, Series B 1972;34(1):1–18.
[20] O'Hagan A. Kendall's advanced theory of statisticsvol. 2B. New York: Wiley; 1994. p. 218–9.
[21] Gelfand AE, Smith AFM. Sampling-based approaches to calculating marginal densities. J Am Stat Assoc 1990;85(410):398–409.
[22] Geman S, Geman D. Stochastic relaxation, Gibbs distributions, and the Bayesian restoration of images. IEEE Trans Pattern Anal Mach Intell 1984;6(6):721–41.
[23] Rowe DB. Modeling both the magnitude and phase of complex-valued fMRI data. NeuroImage 2005;25(4):1310–24.
[24] Rowe DB, Logan BR. A complex way to compute fMRI activation. NeuroImage 2004;23(3):1078–92.
[25] Petridou N, Plenz D, Silva AC, Loew M, Bodurka J, Bandettini PA. Direct magnetic resonance detection of neuronal electrical activity. Proc Natl Acad Sci 2006;103(43):16015–20.
[26] Zhang Z, Romero A, Muckley MJ, Vincent P, Yang L, Drozdzal M. Reducing uncertainty in undersampled MRI reconstruction with active acquisition. CoRR, abs/1902.03051; 2019. http://arxiv.org/abs/1902.03051.
[27] Karaman MM, Bruce IP, Rowe DB. A statistical fMRI model for differential T_2^* contrast incorporating T_1 and T_2^* of gray matter. Magn Reson Imaging 2014;32(1):9–27.
[28] Benjamini Y, Hochberg Y. Controlling the false discovery rate: a practical and powerful approach to multiple testing. J Royal Stat Soc, Series B 1995;57(1):289–300.
[29] Genovese CR, Lazar NA, Nichols TE. Thresholding of statistical maps in functional neuroimaging using the false discovery rate. NeuroImage 2002;15(4):870–8.
[30] Logan BR, Rowe DB. An evaluation of thresholding techniques in fMRI analysis. Neuroimage 2004;22(1):95–108.
[31] Nencka AS, Hahn AD, Rowe DB. The use of three navigator echos in Cartesian EPI reconstruction reduces Nyquist ghosting. In: Proceedings of the 16th Annual Meeting of ISMRM, 3032; 2008.
[32] Hahn AD, Nencka AS, Rowe DB. Enhancing the utility of complex-valued functional magnetic imaging detection of neurobiological processes through postacquisition estimation and correction of dynamic B_0 errors and motion. Hum Brain Mapp 2012;33(2):288–306.
[33] Breuer FA, Blaimer M, Heidemann RM, Mueller MF, Griswold MA, Jakob PM. Controlled aliasing in parallel imaging results in higher acceleration (CAIPIRINHA) for multi-slice imaging. Magn Reson Med 2005;53(3):684–91.
[34] Risk BB, Kociuba MC, Rowe DB. Impacts of simultaneous multislice acquisition on sensitivity and specificity in fMRI. NeuroImage 2018;172:538–53.
[35] Rowe DB, Bruce IP, Nencka AS, Hyde JS, Kociuba MC. Separation of parallel encoded complex-valued slices (SPECS) from a single complex-valued aliased coil image. Magn Reson Imaging 2016;34(3):359–69.
[36] Hernandez-Garcia L, Vazquez AL, Rowe DB. Complex-valued analysis of arterial spin labeling–based functional magnetic resonance imaging signals. Magn Reson Med 2009;62(6):1597–608.